RSC Advances

PAPER

View Article Online
View Journal | View Issue

Cite this: *RSC Adv.*, 2017, **7**, 4152

Preparation and CO_2 adsorption properties of porous carbon from camphor leaves by hydrothermal carbonization and sequential potassium hydroxide activation

Yang Guangzhi,* Ye Jinyu, Yan Yuhua, Tang Zhihong, Yu DengGuang and Yang Junhe*

Received 16th October 2016
Accepted 4th December 2016

DOI: 10.1039/c6ra25303b

www.rsc.org/advances

In this work, porous carbon was prepared from camphor leaves (CLs) by hydrothermal carbonization (HTC) and sequential potassium hydroxide activation. The morphology, porous structure, chemical properties, and CO_2 capture capacity of the produced materials were investigated. The influence of HTC temperature on the material structure and capture capacity was studied. HTC temperature was found to have a major effect on the structure of the products and their CO_2 capture capacity. The porous carbon obtained under HTC temperature of 240 °C exhibits a high ratio of microporosity, a large specific surface area (up to 1633.71 $m^2\ g^{-1}$) and a maximum CO_2 adsorption capacity of 6.63 mmol g^{-1} at 25 °C under 0.4 MPa. The Langmuir isotherm model depicts the equilibrium data much better than the Freundlich isotherm model. The pseudo-first-order kinetic model describes the kinetic data better than the pseudo-second-order kinetic model. Our results demonstrate that the porous adsorbents prepared from CLs provide a feasible option for CO_2 capture with low cost, environmental friendship and high capture capability.

1. Introduction

Recently, serious environmental problems are gaining more and more attention globally, in particular the issue of global warming. The carbon dioxide (CO_2) as a major anthropogenic greenhouse gas has been increasingly released which needs to be addressed ascribe to its detrimental effect on the global warming issues. Carbon capture and storage technology is a potential option to solve this problem. Currently, capturing CO_2 using various porous materials has attracted increasing attention, including materials such as zeolites, mesoporous silica, metal–organic frameworks, molecular sieves and porous carbon, because of their abundant pore structures and high surface area.[1–4] Among these materials, porous carbons have the greatest potential for application because they are derived from a large variety of low-cost resources and have a highly developed porous structure, abundant functional groups, hydrophobicity and high availability.[5–7]

Porous carbons are often derived from various biomasses by thermal pyrolysis, chemical activation or hydrothermal carbonization (HTC), followed by carbonization or chemical activation. Zhu *et al.*[8] investigated the characteristics and tetracycline adsorption behaviour of a novel porous carbon prepared using HTC. High activation temperatures ranging from 300 to 700 °C were found to work well for hydrochar carbonization and the produced materials exhibited high surface areas (>270 $m^2\ g^{-1}$). Wang *et al.*[9] obtained development activated carbon materials with a high specific surface area (over 3000 $m^2\ g^{-1}$) and large pore volume (over 2 $cm^3\ g^{-1}$) using potassium hydroxide (KOH) activation of fossil-based materials. Parshetti *et al.*[10] obtained low-cost carbonaceous adsorbents with a remarkable carbon dioxide uptake capacity (3.71 mmol g^{-1}) from empty palm fruit bunch feedstock using HTC and chemical activation. Zhan *et al.*[11] successfully synthesized composite graphene-based mesoporous silica sheets to serve as an efficient carrier support for polyethyleneimine *via* a nano-casting technology, which exhibited a high adsorption capacity of 190 mg g^{-1} and good cycle stability for CO_2 capture.

An enormous range of biomass materials has been used for activated carbon precursors, including palm seed,[12] rice husk,[13] corn cobs,[14] fruit stone,[15,16] date stone,[17] tomato-peel,[18] cellulose,[19] *Eucalyptus camaldulensis* wood,[20] cotton stalk,[21] and oak leaf.[22] Among these waste biomass materials, leaves are a sustainable resource which do not require the destruction of trees. The camphor tree has leaves all year and is the "city tree" of Shanghai. This tree is widely planted in Shanghai, as well as in many other cities. We can obtain camphor leaves (CLs) anytime, either by picking fresh leaves from the tree or

School of Materials Science and Engineering, University of Shanghai for Science and Technology, Shanghai 200093, China. E-mail: yanggzh@usst.edu.cn; jhyang@usst.edu.cn

collecting fallen ones on the ground. To the best of our knowledge, to date, CLs have not been reported as a precursor material for porous carbon or used as adsorbents for CO_2.

In this work, we have demonstrated a facile method to synthesize porous carbon from CLs under mild conditions using HTC and subsequent chemical activation using KOH. The morphology, porous structure, functional groups and elemental composition of the prepared materials were studied. The CO_2 adsorption performance of the materials was evaluated under a pressure range of 1–4 bar at 25 °C. The adsorption capacity and the adsorption dynamics were investigated, and a possible adsorption isotherm model was proposed.

2. Experimental

Materials

CLs used in this study were obtained locally at the University of Shanghai for Science and Technology by collecting fallen leaves. The raw materials were washed several times using running water and then drenched in deionized water using ultrasonic vibrations to remove impurities, like dirt and flesh. After that, the samples were dried for 24 h at 105 °C, and then cut into pieces with sizes smaller than 5 mm. The samples were then stored at room temperature in a sealed valve bag for further use.

Synthesis of porous carbons

Fig. 1 illustrates the preparation process of porous carbon from CL biomass. Firstly, 3 g samples were completely submerged into 60 ml of deionized water and sealed in an automated stainless-steel hydrothermal reactor with a volume of 100 ml, and then heated to a certain temperature for HTC for 5 h at a 5 °C min^{-1} heating rate. After HTC, the reactor was cooled naturally to room temperature. The resulting hydrochars were then obtained as a solid residue after filtration and were washed repeatedly using distilled water and dried at 105 °C for 12 h. Secondly, the hydrochars were impregnated with KOH solution at a weight ratio of 1 : 3, stirred overnight and then dried. After dryness, the mixture was placed in an alumina-crucible and heated to 800 °C at 3 °C min^{-1} under a N_2 atmosphere and held at this temperature for 1 h. After been cooled to room temperature, the samples were mixed with an excess amount of a 10 wt% HCl solution, stirred overnight, and washed repeatedly using distilled water until the washing solution was neutral. Finally, the wet synthesized materials were dried and stored for further use. Five different HTC temperatures were studied: 180, 210, 240, 270 and 300 °C. The final samples were correspondingly designated as AHTC-180, AHTC-210, AHTC-240, AHTC-270 and AHTC-300 according to the HTC temperature.

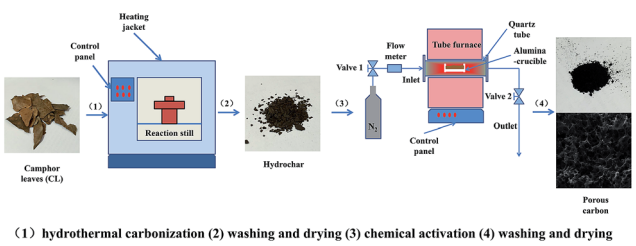

(1) hydrothermal carbonization (2) washing and drying (3) chemical activation (4) washing and drying

Fig. 1 Schematic diagram showing the preparation of porous carbon.

Characterization

The morphologies of the porous carbon materials were investigated using a FEI/Philips XL30 ESEM FEG field emission scanning electron microscopy (SEM) system equipped with an energy dispersive spectrometer (EDS). The surface area and pore volume were determined using N_2 adsorption–desorption isotherms measured at 77 K using a physisorption analyser (Micromeritics, Model ASAP 2020, USA) and determined using the Brunauer–Emmett–Teller (BET) method and *t*-plot method. The pore size distribution and pore volume were derived from the adsorption branch of the isotherm using Density Functional Theory (DFT). The infrared spectra of the porous carbon were recorded using FTIR spectroscopy (VERTEX 70 Fourier transform infrared spectrometer, Bruker, USA). X-ray photoelectron spectroscopy (XPS) measurements were performed using an ESCALAB 250Xi (Thermo Scientific, US) with Al Kα X-ray radiation as the X-ray source for excitation. Transmission electron microscopy (TEM) images were recorded using a Tecnai G2 F30 S-TWIN (FEI, US) with an accelerating voltage of 300 kV.

CO_2 adsorption

Fig. 2 shows a schematic of the experimental instruments used for the CO_2 adsorption/desorption experiments with the synthesized carbon adsorbents. The experimental instruments consist of some valves, a gas mixing section, an adsorption column and an online gas chromatograph.

Switch valves, reduction valves and counterbalance valves were used to ensure the accuracy and stability of gas pressure for each part of the system. Two mass flow controllers (MFC) were used to regulate CO_2 concentration by controlling the flow rates of He and CO_2 gases entering the mixing instrument (100 mm length and 2 mm internal diameter). A thermocouple was set in the middle of the adsorbent bed to detect and control the temperature. The adsorption column is a fixed-bed reactor made up of fused quartz of 384 mm in length and with a 9 mm inner diameter. Adsorbents were loaded inside the fused quartz with some glass wool (DMCS Treated Glass Wool 3352, OHIO VALLEY Specialty Company, USA) placed at the bottom and top

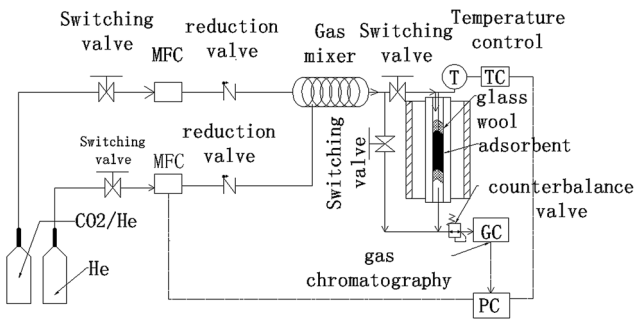

Fig. 2 Schematic diagram of the CO_2 adsorption instrument.

of the adsorbents to insure a fixed and stable state of the powders. The concentrations of CO_2 and He were detected online using a gas chromatograph (GC) analyzer (GC-2014, Shimadzu, Japan). The quartz could be heated to a high temperature for desorption by being placed in a vertical oven.

In the adsorption state, about 1 g of dry adsorbent was loaded. Firstly, a desorption pre-treatment for other gases adsorbed in the adsorbents was implemented at 200 °C with a 25 ml min^{-1} feeding rate of He for 2 h. Secondly, after the adsorption column was cooled down to the required adsorption temperature, the feed gas was switched from He to a CO_2/He mixture (CO_2 volumetric concentration = 10%) for CO_2 adsorption. The mixture feed flow rate was constant at 25 ml min^{-1}. The pressure of the system could be modified from 1 bar to 4 bar for different experiments using a by-pass line of He. Finally, after the adsorption of one pressure was finished, a desorption procedure was performed. And then another adsorption and desorption cycle could be performed again at another pressure.

The CO_2 adsorption capacity Q (mmol g^{-1}) of adsorbents was calculated as follows:

$$Q = \frac{PV_t}{mRT} \quad (1)$$

$$V_t = \int_0^t FC_{con}\mathrm{d}t \quad (2)$$

where P (Pa) is the pressure during the experiment, V_t (ml) is the adsorption volume of each experiment cycle, m (g) is the mass of the adsorbent, R (kPa L K^{-1} mol^{-1}) is the ideal gas constant, T (K) is the temperature, t (min) is the time of each experiment cycle, F (ml min^{-1}) is the gas flow rate and C_{con} is the concentration ratio of CO_2.

3. Results and discussion

Morphology, porous structure, and elemental composition

Fig. 3 shows the SEM images of the synthesized porous carbon, and it clearly demonstrates the formation of randomly distributed pores and cavities. All the samples retained the structure of the CLs in terms of hard tissue with porous characteristics derived from the skeleton crystalline cellulose of the leaves. Different pore sizes and shapes between the particles can be observed on the sample surfaces, which may have been created through the pyrolysis of the CLs and the leaching of potassium during the activation process according to the following stoichiometric redox reaction.[23]

$$6KOH + 2C \rightarrow 2K + 2K_2CO_3 + 3H_2 \quad (3)$$

In contrast, it can be seen that the samples have different amounts of pores and different sizes of fragments, indicating that the temperature of HTC greatly affected the hemicellulose, cellulose, and lignin components of the sample cell walls, which modified the surfaces properties of the adsorbents.[24,25] For example, the AHTC-240 and AHTC-270 samples seem to have smaller fragment sizes than the others. During the HTC process, the CL biomass is partially pyrolyzed and some chemically active points are formed on the surface, which may enhance the activation of KOH and generate pores.[9] For a temperature of activation higher than 700 °C, K_2CO_3 is decomposed to K_2O, which may be further reduced to metallic potassium. This reduced potassium is then removed from the carbon matrix through evaporation (the boiling point of potassium is 762 °C), a proportion of which is also intercalated, resulting in pore formation in the raw material.[26,27] TEM images of AHTC-240 are shown in Fig. 4, which reveal the presence of randomly oriented uniform micropores (white dots in Fig. 4(a) and (b)) with a sponge-like morphology.

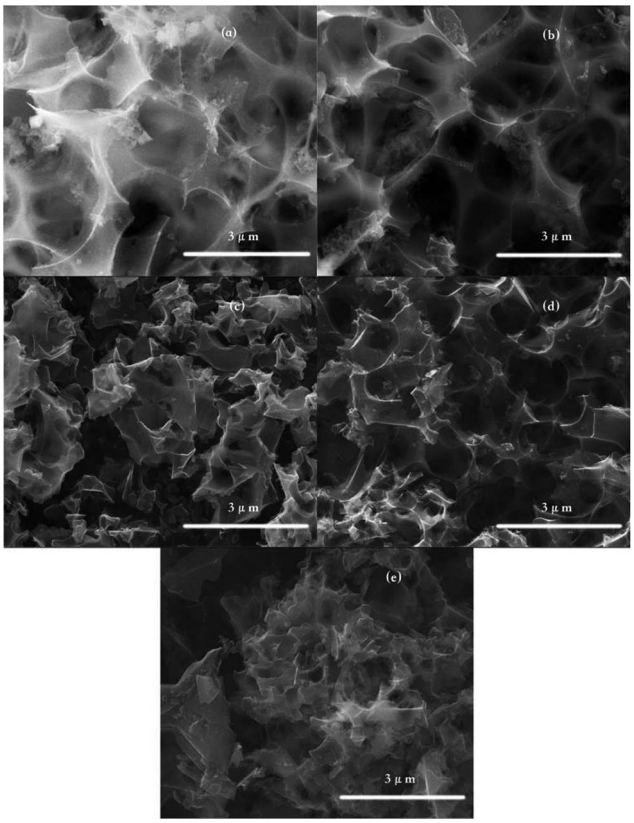

Fig. 3 SEM images of AHTC-180, AHTC-210, AHTC-240, AHTC-270 and AHTC-300 (a, b, c, d and e, respectively).

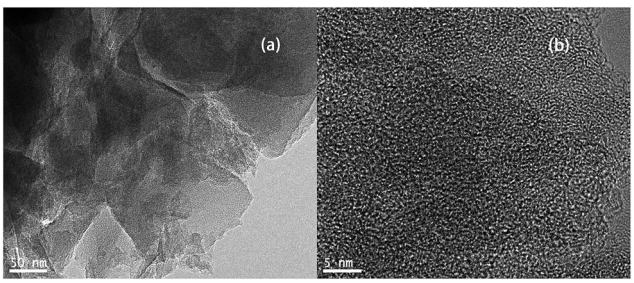

Fig. 4 TEM images of (a) AHTC-240 (10 nm) and (b) AHTC-240 (5 nm).

Table 1 Elemental analysis using EDS

Element	AHTC-180	AHTC-210	AHTC-240	AHTC-270	AHTC-300
C (atom%)	60.10	63.62	65.56	66.11	62.35
N (atom%)	10.49	15.47	13.98	14.23	16.75
O (atom%)	29.41	20.91	20.40	19.62	20.90

Table 2 Yields of HTC and activation processes

Sample	HTC	Yield (wt%) activation	Overall
AHTC-180	69.83	18.69	13.05
AHTC-210	64.17	30.05	19.28
AHTC-240	62.00	41.07	25.46
AHTC-270	56.64	40.83	23.13
AHTC-300	52.10	40.75	21.23

For further investigation, elemental analysis of the carbon adsorbents using EDS was conducted and the results are shown in Table 1. All the samples are rich in carbon because the process combined hydrothermal carbonization and activation.[28] An increasing trend of carbon content when the temperature of HTC increased from 180 to 270 °C is apparent. However, when the temperature is increased to 300 °C, the carbon content is reduced, and this may be due to the secondary decomposition of cellulose under a high hydrothermal temperature.[29] A fluctuation in nitrogen and oxygen content was observed. Significant fluctuations were observed when the HTC temperature was raised from 180 to 210 °C, indicating that HTC affects the element composition greatly when the temperature is elevated to higher than 210 °C.

Table 2 shows the yields of HTC and the activation processes. The yield of hydrochar decreased from 69.83% to 52.10% with an increase in the HTC temperature. KOH activation of the hydrochar precursor resulted in yields in the range of 18.69–41.07%. As a result, the overall yield increased as the temperature increased from 180–240 °C, and decreased when the temperature rise further from 240–300 °C, due to the higher yield of HTC, but a lower yield of activation with an increase of temperature.[30]

The nitrogen adsorption/desorption isotherms of the porous carbon at −196 °C are shown in Fig. 5. The BET surface area, pore volume and average pore size of the prepared samples are listed in Table 3. The adsorption isotherm of all the samples exhibited a combined type 1 and type 4 behavior according to the IUPAC (International Union of Pure and Applied Chemistry). A type 1 isotherm with a narrow knee at low relative pressure (P/P_0 < 0.1) can be associated with a microporous structure, while a type 4 isotherm with a hysteresis loop at a relative pressure around 0.8 is usually associated with the filling and emptying of mesoporous structures through capillary condensation. Thus, the porosity of all samples was mainly microporous and mesoporous in nature. Generally, in a low relative pressure (P/P_0 < 0.1) range, with the abrupt rising of the isotherm, microporous pores dominate in the pore diameter

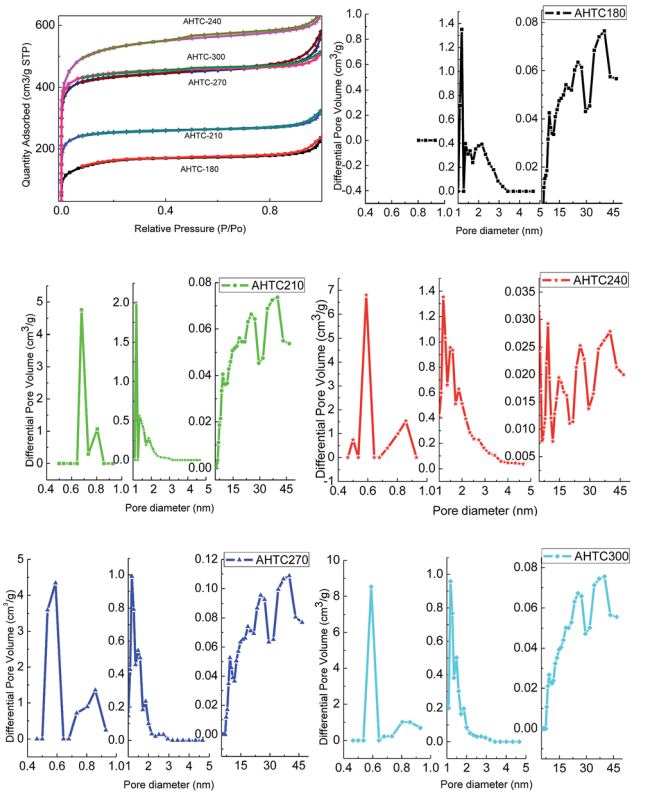

Fig. 5 N_2 adsorption–desorption isotherms and pore size distribution of the porous carbon at 77 K at various HTC temperatures.

distribution. AHTC-240 has the highest microporous (1083.57 $m^2 g^{-1}$) and total (1633.71 $m^2 g^{-1}$) BET surface areas, and the reason for this may be that the HTC treatment resulted in special surface roughness, functional groups, carbon content and carbon groups, which affected the following activation reaction in terms of an increase of surface area and porosity.[12,31] It can be concluded that the temperature of HTC plays a key role in the formation of a porous texture; therefore, it is critical in defining optimal HTC conditions.[24] However, the BET surface area increased as the temperature increased from 180–240 °C, but decreased with a further rise of temperature from 240–300 °C. This phenomenon was mainly caused by different fractions of carbon in the solid-phase. The fraction of carbon present in the solid-phase is influenced by the reaction temperature during HTC. The gas evolution *via* decarboxylation and volatilization of organics is increased at higher temperatures, and thus low retention of carbon in the solid-phase is retained at higher temperatures.[32] Therefore, AHTC-240 showed the largest specific surface area (1633.71 $m^2 g^{-1}$) and highest total pore volume (0.57 $cm^3 g^{-1}$) among all the carbon samples, suggesting that the HTC treatment at 240 °C followed by chemical activation with KOH at 800 °C represents the optimized experimental conditions for the synthesis of porous carbon from the waste CL biomass.

Structure characterization

Qualitative analysis of the functional groups on the porous carbon was carried out using FTIR spectroscopy as shown in

Table 3 BET characteristics of the porous carbons

Samples	S_{BET}[a] ($m^2\ g^{-1}$)	V_{total}[b] ($cm^3\ g^{-1}$)	S_{micro}[c] ($m^2\ g^{-1}$)	V_{micro}[c] ($cm^3\ g^{-1}$)	D_p[d] (nm)
AHTC-180	514.98	0.37	192.65	0.11	2.84
AHTC-210	773.63	0.50	601.72	0.32	2.59
AHTC-240	1633.71	0.98	1083.57	0.58	2.41
AHTC-270	1322.58	0.90	1061.31	0.56	2.71
AHTC-300	1350.79	0.79	1128.14	0.59	2.35

[a] BET surface area. [b] Total pore volume measure at $P/P_0 = 0.99$. [c] Micropore surface area and micropore volume estimated $d < 2$ nm using DFT. [d] Average pore diameter.

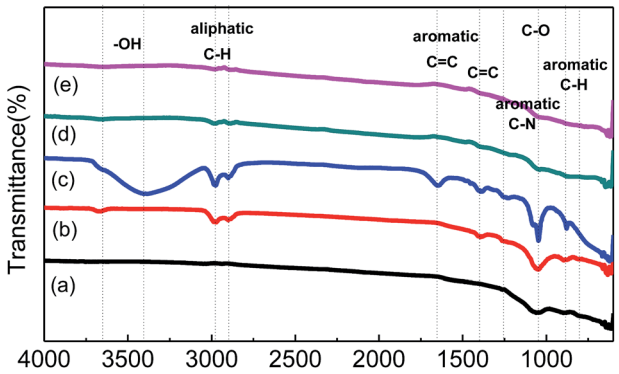

Fig. 6 FTIR spectra of AHTC-180 (a), AHTC-210 (b), AHTC-240 (c), AHTC-270 (d) and AHTC-300 (e).

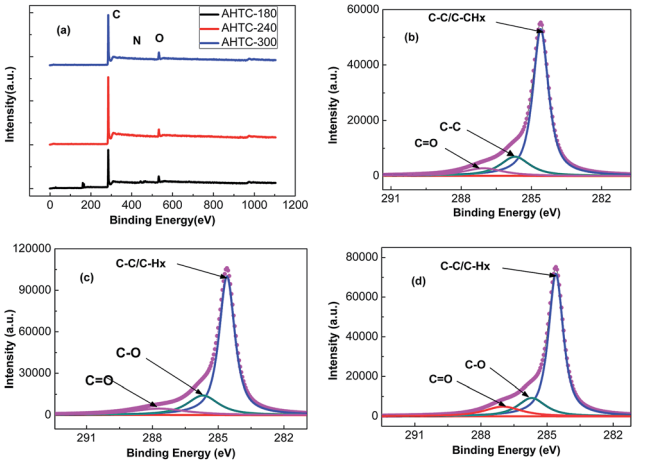

Fig. 7 C 1s XPS spectra of AHTC-180 (a), AHTC-240 (b), AHTC-300 (c) and O 1s XPS spectra of the prepared porous carbons (d).

Fig. 6. The peak observed at 1047 cm^{-1} represents the C–O stretch in cellulose and hemicellulose in the cell walls. The peaks at 886 and 802 cm^{-1} are aromatic C–H out of plane deformation in a mono-substituted benzene ring. For AHTC-210, additional peaks appeared at 3600, 2979, 2896, 1400 and 1257 cm^{-1}, which correspond to –OH bending of carboxylic acids, C–H stretching of alkanes, C=C stretching of conjugated alkene and C–N stretching vibration, respectively. For AHTC-240, these stretching vibrations became stronger and the residual lignin (aromatic C=C vibration at 1400 cm^{-1}) was retained. In addition, greater aromatic C=C stretching vibrations (1600 cm^{-1}) were observed, and further evidence for aromatic C was provided with the appearance of the peaks at 1047, 886 and 802 cm^{-1}. Interestingly, these peaks were dramatically diminished in AHTC-270 and completely absent at 300 °C, possibly due to the decomposition of lignin and the hydrolysis of cellulose under high temperatures (250–350 °C) during the HTC process. However, during HTC at relatively lower temperatures (180–240 °C), the majority of the hemicellulose and other water-soluble organic compounds leached out from the CLs and were dissolved in water. Therefore, the rest of the cellulose and lignin components maintained most of their functional groups.

XPS was then used to determine the surface chemical properties of the as-prepared carbon materials. The wide XPS spectra (Fig. 7(a)) confirmed three peaks, at 284.8, 401.3 and 533.4 eV, corresponding to C 1s, N 1s, and O 1s, respectively. To understand the electronic states of the elements in the porous carbon materials, we paid more attention to the higher-resolution spectra (Fig. 7(b)–(d)). The high-resolution C 1s photoelectron spectra for the as-prepared samples include three common signals at 284.6, 286.1 and 287.0 eV,[33] which can be attributed to the aliphatic/aromatic carbon groups (C–Hx, and C–C), hydroxyl groups (C–O–H), and carbonyl groups (C=O), respectively. As shown in Table 4, large amounts of carbon were detected in all samples, which agreed well with the previous EDS analysis.

Table 4 The elemental analysis using XPS

Element	AHTC-180	AHTC-240	AHTC-300
C (atom%)	89.44	92.69	90.66
O (atom%)	9.92	6.65	8.56
N (atom%)	0.64	0.66	0.78

CO_2 adsorption studies

The CO_2 adsorption capacities (q_e) of the porous carbon materials were investigated at 25 °C under a pressure of 1 bar as shown in Fig. 8. With the increase of HTC temperature from 180 °C to 240 °C, the q_e was found to increase significantly and reached a maximum value of 0.80 mmol g^{-1} for AHTC-240. However, the adsorption capacity decreased when the temperature of the HTC rose from 270 °C to 300 °C. It was found that

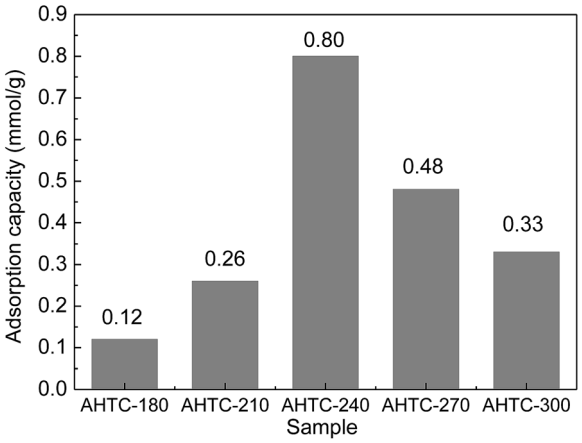

Fig. 8 CO_2 adsorption capacity of synthesized adsorbents at 1 bar and 25 °C.

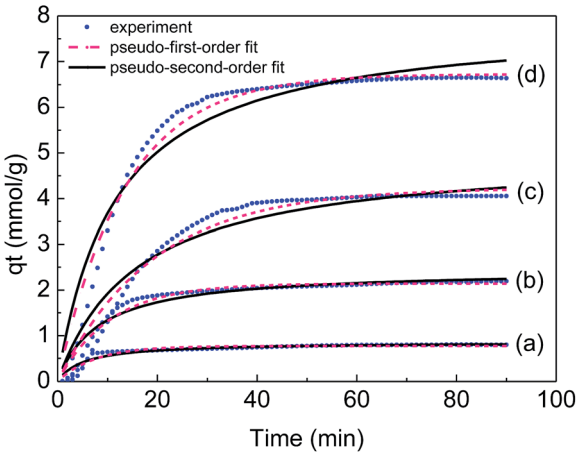

Fig. 9 Experimental CO_2 uptake on AHTC-240 and corresponding fit to kinetic models at pressures of 1 bar (a), 2 bar (b), 3 bar (c) and 4 bar (d).

Table 5 CO_2 adsorption capacity of the porous carbon materials

CO_2 pressure (bar)	AHTC-180	AHTC-210	AHTC-240	AHTC-270	AHTC-300
1	0.12	0.33	0.80	0.48	0.33
2	1.24	1.43	2.19	1.51	1.22
3	1.94	2.26	4.05	3.25	2.64
4	2.45	2.68	6.63	4.09	3.50

the equilibrium CO_2 uptake of the synthesized adsorbents decreased in the following order: AHTC-240 > AHTC-270 > AHTC-300 > AHTC-210 > AHTC-180 (Table 5). Based on the preliminary investigation of the materials, the different adsorption capacities were mostly attributed to the different quantity and type of functional group of the carbonaceous material (Fig. 6), along with the specific surface area, microporosity and total volume (Table 3). Consequently, AHTC-240, which had the highest amounts and most diverse distribution of functional groups and the largest specific surface area and total volume, showed the highest CO_2 adsorption capacity among all the samples: 2.19, 5.54 and 6.63 mmol g^{-1} at 2, 3 and 4 bar, respectively.

To investigate the kinetics of CO_2 adsorption, the isotherm of AHTC-240 in the present work was fitted using two kinetic models, namely, pseudo-first-order and pseudo-second-order models. The pseudo-first-order equation was applied to determine the kinetic parameters:

$$q_t = q_e(1 - e^{-k_1 t}) \quad (4)$$

where q_t and q_e (mmol g^{-1}) are adsorption capacities at time t (min) and at equilibrium respectively and k_1 (min^{-1}) is the kinetic rate constant of the pseudo-first-order kinetic model.

The pseudo-second-order equation[34] is expressed as:

$$q_t = \frac{q_e^2 k_2 t}{1 + q_e k_2 t} \quad (5)$$

where k_2 (g $mmol^{-1}$ s^{-1}) is the rate constant of second-order-adsorption.

Each model's adequacy was determined using the coefficient of determination (R^2) and an error (error%), which is based on the normal standard deviation (according to ref. 35). Error% showed the fit between the experimental and model predicted data.

$$R^2 = 1 - \frac{\sum_{N-1}^{N} \left(q_{t\cdot \exp\cdot N} - q_{t\cdot \mathrm{pred}\cdot N}\right)^2}{\sum_{N-1}^{N} \left(q_{t\cdot \exp\cdot N} - \overline{q_{t\cdot \exp\cdot N}}\right)^2} \quad (6)$$

$$\text{Error } (\%) = \sqrt{\frac{\sum \left[\left(q_{t(\exp)} - q_{t(\mathrm{pred})}\right) / q_{t(\exp)}\right]^2}{N-1}} \times 100 \quad (7)$$

Here error%, $q_{t\cdot \exp}$ and $q_{t\cdot \mathrm{pred}}$ (mmol g^{-1}) are the error function, experimental and predicted adsorption capacities from the model at time t, and N is the number of observations.

Fig. 9 shows experimental CO_2 uptake as a function of time on the prepared adsorbents and the corresponding profiles obtained from the two-species adsorption kinetic models for

Table 6 Kinetic parameters for adsorption of CO_2 onto AHTC-240 at different pressures

		Pressure (bar)			
Kinetic model	Parameters	1	2	3	4
Pseudo-first-order	k_1 (min^{-1})	0.1331	0.0947	0.0524	0.0740
	q_e (mmol g^{-1})	0.77	2.14	4.23	6.72
	R^2	0.9159	0.9622	0.9620	0.9744
	Error%	2.11	3.61	7.55	0.12
Pseudo-second-order	k_2 (min^{-1})	0.2157	0.0491	0.0125	0.0109
	q_e (mmol g^{-1})	0.86	2.45	5.00	7.92
	R^2	0.9199	0.9315	0.9255	0.9348
	Error%	3.01	4.69	9.99	6.49

Table 7 Isotherm constants for CO_2 adsorption on the synthesized adsorbents

	Langmuir			Freundlich		
Samples	q_m (mmol g^{-1})	K_L (1 kPa^{-1} mmol^{-1})	R^2	K_F (mmol g^{-1}) (kPa^{-1})$^{1/n}$	n	R^2
AHTC-180	2.73	0.04	0.9812	0.45	1.26	0.9151
AHTC-210	3.13	0.00	0.9999	0.61	1.11	0.9278
AHTC-240	7.86	0.04	0.9423	1.01	1.40	0.9249
AHTC-270	5.71	0.03	0.9787	0.64	1.37	0.9598
AHTC-300	5.05	0.01	0.9920	0.48	1.46	0.9717

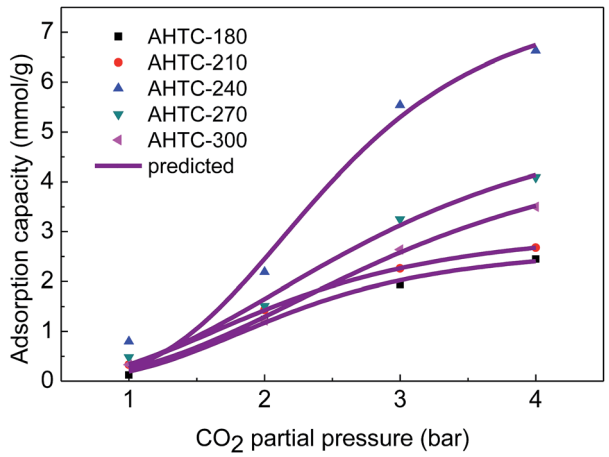

Fig. 10 Experimental and Langmuir model predicted equilibrium CO_2 uptakes on the synthesized absorbents.

CO_2 adsorption on AHTC-240 at different pressure. It is clearly shown that the pseudo-second-order model underestimated the CO_2 uptake up to 60 min and after this point it continually overestimated the CO_2 uptake until the process approached equilibrium. In addition, the pseudo-first-order kinetic model was in good agreement with the experimental data during the whole experimental process. This further based on the higher R^2 values and lower error% values, the pseudo-first-order model better expressed the kinetics data of CO_2 adsorption onto AHTC-240 compared with those from the pseudo-second-order model (Table 6). The transportation mode of CO_2 molecules on the carbon surface depicts the first-order nature of the adsorption process and according to first-order kinetics, the rate of diffusion of CO_2 into the adsorbent surface is faster than the occurrence of chemical reactions on the surface.[5]

However, the fitting of the experimental equilibrium data to the mathematical models could actually interpretive the results in this study. Therefore, isotherm equilibrium data were analysed by using nonlinear Langmuir and Freundlich models to evaluate the behaviour of CO_2 molecules toward synthesized adsorbents.

The Langmuir isotherm describes the monolayer adsorption process on uniform adsorption sites, and can be expressed as:

$$q_e = \frac{q_m K_L C_e}{1 + K_L C_e} \quad (8)$$

where q_m (mmol g^{-1}) and K_L (kPa mmol^{-1}) are the Langmuir constants that are correlated to the adsorption capacity and adsorption rate, respectively.

The Freundlich isotherm describes the multilayer adsorption process on heterogeneous adsorption sites, and can be expressed as:

$$q_e = K_F C_e^{1/n} \quad (9)$$

Table 8 The adsorbent performance of some typical carbon materials in the literature

Precursor	S_{BET} (m^2 g^{-1})	V_{total} (cm^3 g^{-1})	V_{micro} (cm^3 g^{-1})	C_{CO_2} (mol%)	Temperature (°C)	Pressure (bar)	CO_2 adsorption (mmol g^{-1})	Ref.
White wood	1400	0.62	—	10	25	1	0.61	36
Hexamethoxymethyl–melamine	463	0.48	0.09	10	30	1	0.53	5
Melamine–formaldehyde resin	266	—	0.03	10	30	1	0.78	37
Oil-based pitch	1720	0.98	0.64	100	25	1	1.90	38
Oil cake/walnut shell	1080	0.46	0.58	100	25	1	0.77	39
Recycled polyethylene terephthalate	418	0.20	0.16	100	25	1	1.09	40
Olive stones/almond shells	1113	0.51	0.45	100	25	0.15	1.02	41
Horse manure	749	0.816	0.141	100	0	0.1	1.36	42
AHTC-240	1633	0.98	0.58	10	25	1	0.80	This work

where K_F and n are Freundlich constants, K_F (mmol g^{-1}) $(kPa^{-1})^{1/n}$ and n represents the adsorption capacity and $1/n$ indicates the adsorption intensity and curvature $1/n < 1$ represents a normal Langmuir isotherm, whereas $1/n > 1$ indicates cooperative adsorption. Parameters of the above adsorption isotherm models and correlation coefficients (R^2) were obtained using nonlinear regression of the experimental data with the aid of OriginPro 8 software, and are given in Table 7. The experimental data and Langmuir model predicted equilibrium CO_2 uptake are shown in Fig. 10. Freundlich isotherm models closely describe the CO_2 adsorption equilibrium data but the best fit is obtained using the Langmuir isotherm model as indicated by the higher correlation coefficient (R^2). The best fit obtained using the Langmuir isotherm model suggests an energetically heterogeneous adsorbent surface. The Freundlich model constant n was $1 < n < 10$ for all the adsorbents, suggesting that the CO_2 adsorption onto the porous carbon can be considered to be favorable.[43] The Langmuir model parameter q_m indicates maximum monolayer adsorption capacity and it is coordinated with surface area and porosity, indicating that the uptake of CO_2 by the synthesized carbon adsorbents mostly occurred in the form of physical adsorption. Table 8 shows a comparison of the adsorbent performance of some typical porous carbon materials reported in literature. The as-prepared materials show some advantages in CO_2 adsorption performance.

4. Conclusions

In this study, major microporous CL-based porous carbon was successfully prepared by combining HTC and KOH activation, and was demonstrated to be a promising material for CO_2 capture. The effect of HTC temperature on the products was studied and was found to have a major effect on the preparation process. AHTC-240 exhibited the largest specific surface area (up to 1633.71 $m^2 g^{-1}$), the highest total pore volume (0.98 $cm^3 g^{-1}$) and microporosity (0.58 $cm^3 g^{-1}$). As for CO_2 adsorption, it had a fast CO_2 uptake rate and a high capacity of 0.80 mmol g^{-1} at 1 bar pressure and 6.63 mmol g^{-1} at 4 bar and 25 °C. Overall, porous carbon materials derived from CLs possess low regeneration cost, long-term stability for CO_2 capture and easy regeneration conditions. Therefore, the porous carbon materials derived from CL biomass *via* hydrothermal carbonization and chemical activation have a potential use in carbon capture and storage.

Acknowledgements

We gratefully acknowledge the support of the National Science Foundation of China (51102169, 51272157, 51102168), Shanghai Nature Science Foundation (16ZR1423400) and the Hujiang Foundation of China (B14006).

References

1 A. Vinu, C. Streb, A. V. Murugesan and M. Hartmann, *J. Phys. Chem. B*, 2003, **107**, 8297–8299.
2 N. Hedin, L. Andersson, L. Bergström and J. Yan, *Appl. Energy*, 2013, **104**, 418–433.
3 M. Kacem, M. Pellerano and A. Delebarre, *Fuel Process. Technol.*, 2015, **138**, 271–283.
4 S. Keskin, T. M. Van Heest and D. S. Sholl, *ChemSusChem*, 2010, **3**, 879–891.
5 C. Goel, H. Kaur, H. Bhunia and P. K. Bajpai, *J. CO_2 Util.*, 2016, **16**, 50–63.
6 W. M. Hao, E. Bjorkman, M. Lilliestrale and N. Hedin, *Appl. Energy*, 2013, **112**, 526–532.
7 M. G. Plaza, C. Pevida, B. Arias, M. D. Casal, C. F. Martin, J. Fermoso, F. Rubiera and J. J. Pis, *J. Environ. Eng.*, 2009, **135**, 426–432.
8 X. Zhu, Y. Liu, C. Zhou, G. Luo, S. Zhang and J. Chen, *Carbon*, 2014, **77**, 627–636.
9 J. C. Wang and S. Kaskel, *J. Mater. Chem.*, 2012, **22**, 23710–23725.
10 G. K. Parshetti, S. Chowdhury and R. Balasubramanian, *Fuel*, 2015, **148**, 246–254.
11 S. B. Yang, L. Zhan, X. Y. Xu, Y. L. Wang, L. C. Ling and X. L. Feng, *Adv. Mater.*, 2013, **25**, 2130–2134.
12 M. A. Islam, I. A. W. Tan, A. Benhouria, M. Asif and B. H. Hameed, *Chem. Eng. J.*, 2015, **270**, 187–195.
13 W. J. Liu, F. X. Zeng, H. Jiang and X. S. Zhang, *Bioresour. Technol.*, 2011, **102**, 8247–8252.
14 N. Bagheri and J. Abedi, *Chem. Eng. Res. Des.*, 2009, **87**, 1059–1064.
15 A. F. Martins, A. L. Cardoso, J. A. Stahl and J. Diniz, *Bioresour. Technol.*, 2007, **98**, 1095–1100.
16 Y. Nakagawa, M. Molina-Sabio and F. Rodríguez-Reinoso, *Microporous Mesoporous Mater.*, 2007, **103**, 29–34.
17 F. Bouhamed, Z. Elouear and J. Bouzid, *J. Taiwan Inst. Chem. Eng.*, 2012, **43**, 741–749.
18 E. Sabio, A. Álvarez-Murillo, S. Román and B. Ledesma, *Waste Manage.*, 2016, **47**, 122–132.
19 M. Sevilla, A. B. Fuertes and R. Mokaya, *Energy Environ. Sci.*, 2011, **4**, 1400–1410.
20 A. Heidari, H. Younesi, A. Rashidi and A. A. Ghoreyshi, *J. Taiwan Inst. Chem. Eng.*, 2014, **45**, 201–228.
21 A. N. A. Elhendawy, A. J. Alexander, R. J. Andrews and G. Forrest, *J. Anal. Appl. Pyrolysis*, 2008, **82**, 272–278.
22 B. Hu, S. H. Yu, K. Wang, L. Liu and X. W. Xu, *Dalton Trans.*, 2008, 5414–5423.
23 M. A. Lillo-Ródenas, D. Cazorla-Amorós and A. Linares-Solano, *Carbon*, 2003, **41**, 267–275.
24 M. A. Islam, I. A. W. Tan, A. Benhouria, M. Asif and B. H. Hameed, *Chem. Eng. J.*, 2015, **270**, 187–195.
25 G. Pari, S. Darmawan and B. Prihandoko, in *4th International Conference on Sustainable Future for Human Security Sustain 2013*, ed. N. A. Utama, B. McLellan, S. Hamzah, A. Trihartono, H. Suryatmojo, S. Widodo, M. E. Wijaya, S. K. Himmi, M. Esteban, H. Farzaneh, N. Prilandita, N. Susan, H. Huboyo, M. Nurudin and Y. Prihatmaji, Elsevier Science Bv, Amsterdam, 2014, vol. 20, pp. 342–351.
26 H. Y. Hsiao, C. M. Huang, M. Y. Hsu and H. Chen, *Sep. Purif. Technol.*, 2011, **82**, 19–27.

27 A. Robau-Sánchez, A. Aguilar-Elguézabal and J. Aguilar-Pliego, *Microporous Mesoporous Mater.*, 2005, **85**, 331–339.
28 R. K. Garlapalli, B. Wirth and M. T. Reza, *Bioresour. Technol.*, 2016, **220**, 168–174.
29 Y. Gao, H.-P. Chen, J. Wang, T. Shi, H.-P. Yang and X.-H. Wang, *J. Fuel Chem. Technol.*, 2011, **39**, 893–900.
30 B. Hu, K. Wang, L. Wu, S. H. Yu, M. Antonietti and M. M. Titirici, *Adv. Mater.*, 2010, **22**, 813–828.
31 I. A. Tan, A. L. Ahmad and B. H. Hameed, *J. Hazard. Mater.*, 2008, **153**, 709–717.
32 X. W. Lu, P. J. Pellechia, J. R. V. Flora and N. D. Berge, *Bioresour. Technol.*, 2013, **138**, 180–190.
33 M. Sevilla and A. B. Fuertes, *Chem.–Eur. J.*, 2009, **15**, 4195–4203.
34 Y. S. Ho and G. McKay, *Process Biochem.*, 1999, **34**, 451–465.
35 R. Serna-Guerrero and A. Sayari, *Chem. Eng. J.*, 2010, **161**, 182–190.
36 S. Shahkarami, R. Azargohar, A. K. Dalai and J. Soltan, *J. Environ. Sci.*, 2015, **34**, 68–76.
37 C. Goel, H. Bhunia and P. Bajpai, *J. Environ. Sci.*, 2015, **32**, 238–248.
38 N. Díez, P. Álvarez, M. Granda, C. Blanco, R. Santamaría and R. Menéndez, *Chem. Eng. J.*, 2015, **281**, 704–712.
39 E. David and J. Kopac, *J. Anal. Appl. Pyrolysis*, 2014, **110**, 322–332.
40 A. Arenillas, F. Rubiera, J. B. Parra, C. O. Ania and J. J. Pis, *Appl. Surf. Sci.*, 2005, **252**, 619–624.
41 A. S. González, M. G. Plaza, F. Rubiera and C. Pevida, *Chem. Eng. J.*, 2013, **230**, 456–465.
42 W. Hao, E. Björkman, M. Lilliestråle and N. Hedin, *Appl. Energy*, 2013, **112**, 526–532.
43 K. Fytianos, E. Voudrias and E. Kokkalis, *Chemosphere*, 2000, **40**, 3–6.

